Supporting Information for "Fluctuations of the Atlantic North Equatorial Undercurrent and associated changes in oxygen transports"

K. Burmeister[1], J. F. Lübbecke[2,3], P. Brandt[2,3], M. Claus[2,3], and J. Hahn[2]

[1]SAMS, Scottish Marine Institute, Oban, Argyll, PA37 1QA, United Kingdom

[2]GEOMAR Helmholtz Centre for Ocean Research Kiel, Düsternbrooker Weg 20, 24105 Kiel, Germany

[3]Christian-Albrechts-Universität zu Kiel, Christian-Albrechts-Platz 4, 24118 Kiel, Germany

Contents of this file

Text S1 to S3, Figures S1 to S7 and Table S1.

Introduction

In section S1 of the Supporting Information we give an detailed overview about the processing of the moored and shipboard observations. Section S2 presents details of the estimation of eastward transports from zonal velocity observations, their accuracies and uncertainties as well as their associated spatial patterns. In section S3 we investigate the relation between the NEUC transport and zonal wind stress in the tropical Atlantic.

S1: Moored and shipboard observations

Moored data

For our analysis we used velocity, hydrography and oxygen data from moorings at 5°N/23°W (Jul 2006-Feb 2008, Nov 2009-Jan 2018), 4.6°N/23.4°W (Nov 2012-Apr 2014) and 4.5°N/22.4°W (Nov 2012-Apr 2014). At all three mooring positions horizontal velocity was measured with downward (Jul 2006-Feb 2008) or upward (Nov 2009-Jan 2018) looking 75-kHz Longranger Acoustic Doppler Current Profilers (ADCPs). The ADCP configuration was set to a sampling period of 2 h, a bin length of 16 m and an ensemble number of 20 pings. A single velocity data point has a standard error of 1.7 $\mathrm{cm\,s^{-1}}$. Given the manufacturer's compass accuracy of 2°, we inferred a velocity error of < 4 % of the absolute measured velocity (Hahn et al., 2014). The minimum measurement range of all mooring periods is 85 m to 755 m. The moored velocity data was linearly interpolated onto a regular time-depth grid (12 h $\times$10 m), and a 40-h low-pass Butterworth filter was applied to remove the tidal signal from the time series (Fig. S1).

Eight pairs of oxygen (AADI Aanderaa optodes of model types 3830 and 4330) and Conductivity-Temperature-Depth (CTD) sensors (Sea-Bird SBE37 microcats) were installed at the moorings evenly distributed in the depth range from 100 m to 800 m. This configuration allows an appropriate estimate of the dissolved oxygen on density surfaces. All instruments were set to a sampling period of 2 h or shorter. The oxygen and CTD sensors were calibrated against CTD casts performed directly prior to or after the deployment period of the mooring. The oxygen sensors were additionally calibrated against laboratory measurements to expand the range of reference calibration points. For more details of the oxygen calibration see Hahn et al. (2014). The root mean square error

of moored temperature, salinity and dissolved oxygen measurements was about 0.003°C, 0.006 and 3 μmol kg^{-1}, respectively (see Hahn et al., 2017). The point measured hydrography and oxygen data was interpolated onto a 12-h time grid.

Shipboard data

24 meridional velocity and 15 hydrographic and oxygen sections between 21°W and 26°W were obtained during cruises between 2002 to 2018 (Table S1). All ship sections cover at least the upper 350 m between 0° and 10°N. The velocity, hydrographic and oxygen ship sections used in this study are an extension of the data set used in Burmeister et al. (2019).

Velocity data were acquired by vessel-mounted ADCPs (vm-ADCPs). Vm-ADCPs continuously record velocities throughout a ship section and the accuracy of 1-h averaged data is better than 2-4 cm s^{-1} (Fischer et al., 2003). Hydrographic and oxygen data obtained during CTD casts were typically performed on a uniform latitude grid with half-degree resolution. The data accuracy for a single research cruise is generally assumed to be better than 0.002°C, 0.002 and 2 μmol kg^{-1} for temperature, salinity, and dissolved oxygen, respectively (Hahn et al., 2017). The single velocity, hydrographic and oxygen ship section were mapped on a regular grid (0.05° latitude × 10 m) and were smoothed by a Gaussian filter (horizontal and vertical influence (cutoff) radii: 0.05° (0.1°) latitude and 10 m (20 m), respectively). The single sections were averaged at each grid point to derive mean sections, which are again smoothed by the Gaussian filter. For the mean velocity, temperature, salinity and oxygen sections the standard error in the NEUC region

(65 − 270 m depth, 3° − 6.5°N) are 1.7 cm s^{-1}, 0.22°C, 0.02 and 3.8 μmol kg^{-1}, respectively.

S2: NEUC transport calculations

Path following algorithm

We derived estimates of the NEUC transport from the 24 meridional ship sections based on the algorithm of Hsin and Qiu (2012) which we consider as a reference NEUC transport. First, the central position Y_{CM} of the current is estimated using the concept of center of mass:

$$Y_{CM}(t) = \frac{\int_{Z_l}^{Z_u} \int_{Y_S}^{Y_N} y\ u(y,z,t)\ dy\ dz}{\int_{Z_l}^{Z_u} \int_{Y_S}^{Y_N} u(y,z,t)\ dy\ dz}, \tag{1}$$

where y is latitude, u is zonal velocity, z is depth, t is time, Z_u (Z_l) is upper (lower) boundary of the flow, and $Y_N = 6$°N ($Y_S = 3.5$°N) is the northern (southern) limit of the current core. We estimated a mean NEUC central position of 4.9°N and a standard deviation of ±0.3°.

Now the eastward velocity is integrated within a box whose meridional range is given by $Y_{CM}(t)$ and the southern (B_S) and northern (B_N) extent of the flow:

$$INT(t) = \int_{Z_l}^{Z_u} \int_{Y_{CM}-B_S}^{Y_{CM}+B_N} u(y,z,t)\ dy\ dz \tag{2}$$

For the integration we used the same boundary conditions as Burmeister et al. (2019). Z_u is the depth of the 24.5 kg m^{-3} and Z_l the depth of the 26.8 kg m^{-3} neutral density surface. The southern boundary is choosen as $Y_{CM} - 1.5$° and the northern boundary is $Y_{CM} + 1.0$°. Note that, if no hydrographic measurements are available for a single ship

section, the neutral density field derived from the mean hydrographic section is used.

Transport reconstruction

The eastward transport associated with the NEUC at about 23°W is computed using moored velocity data at 5°N, 23°W (2006-2018) as well as 4.6°N, 22.4°W (Nov. 2012-Apr. 2014) and 4.5°N, 23.4°W (Nov. 2012-Apr. 2014) combined with 24 meridional ship sections between 21°W and 26°W (Fig S1). In the main manuscript we reconstruct the NEUC transport using the optimal width (OW) method as described in Brandt et al. (2014). We chose this simple method because it is sufficient to represent the NEUC variability and more complex methods do not add any value, which we will show in this section. We validate the OW method using another approach from Brandt et al. (2014) based on Hilbert empirical orthogonal functions (HEOFs).

In the second approach the meridional sections of zonal velocity are reconstructed from the moored zonal velocities by interpolation and extrapolation using data taken at the mooring position. For the reconstruction of meridional sections we use variability patterns derived from the 24 meridional ship sections. Therefore we calculate HEOF pattern from the velocity sections between 4.25°N and 5.25°N, 65 m and 270 m (black dashed frame in Fig. S1). Here, a Hilbert transformation is applied to the zonal velocity fields before an EOF analysis is performed. The advantage of an HEOF is that the statistical patterns efficiently reveal spatial propagation features as for example a meridional migration of the current, in contrast to a traditional EOF. The first HEOF pattern explains 56% of variability contained in the ship section. The real pattern of the first HEOF shows a homogeneous change of velocities over the complete integration area (Fig. S3). Using

only the first HEOF patterns to interpolate between the mooring positions by regressing the patterns onto the moored zonal velocity observations results in similar reconstructed transports as the OW method (black and red line in Fig. S4). As the homogeneous structure of the first HEOF explains most of the variability, there is no added value by including more HEOF patterns to reconstruct the NEUC transport. Nevertheless we want to mention here that the second pattern with a explained variance of 20% describes a meridional shift of the NEUC. A vertical shift of the NEUC might be described by the patterns of the third and fourth HEOF.

To investigate whether the dominant pattern of the first HEOF of the zonal velocities between 4.25°N and 5.25°N represents a meridional migration of the NEUC out of the calculation area the HEOF method is repeated using the zonal velocities between 3.5°N and 6.0°N. This region covers the southern and northern boundary of the NEUC even if the current is meridionally migrating. The fixed box integrated transports for this region calculated from the ship sections (gray squares in Fig. S4) agrees well with the reference transports. Again, the real pattern of the first HEOF shows a homogeneous change of zonal velocity although it explains less variability compared to the first HEOF of the smaller box. Furthermore, the first and second pattern which explain together 66% of the velocity variability seem to describe a meridional shift of the current. Nevertheless, the eastward transport time series reconstructed using the first (yellow line in Fig. S4) or the first two HEOF pattern (blue line in Fig. S4) of zonal velocities between 3.5°N and 6.0°N agrees well with that reconstructed from velocities between 4.25°N and 5.25°N. The mean transport estimates using the bigger box is 1.9 Sv.

In summary, the reconstructed eastward transports between 4.25°N and 5.25°N tend to underestimate the mean current strength of the NEUC, however the time series is able to capture the NEUC variability reasonably well. We choose the smaller box to reconstruct the NEUC transport variability due to the smaller uncertainty of the reconstructed transports when using only the mooring at 5°N, 23°W.

S3: NEUC and sea surface winds

Auxiliary data

Monthly mean JRA-55 surface wind velocities (U_h, Kobayashi et al., 2015) on a 1.25°×1.25° horizontal grid for the time period from 2006 to 2018 are used in this study. We calculated the wind stress τ_h from the JRA-55 reanalysis data using the Bulk formula $\tau_h = \rho_{air} C_D |U_h| U_h$, where $\rho_{air} = 1.22 \mathrm{kg\,m^{-3}}$ is the density of air, $C_D = 0.0013$ is the wind drag coefficient and $|U_h|$ is the absolute value of U_h.

Furthermore, we are using monthly mean wind stress from the ASCAT on METOP Level 4 Daily Gridded Mean Wind Fields (Bentamy & Fillon, 2012). The dataset has a horizontal resolution of 0.25° covering the time period from April 2007 to May 2018. For comparison, ASCAT wind stress data are regridded onto the horizontal grid of the JRA-55 reanalysis data (1.25°) by bin averaging.

Linear regression

We performed a lead-lag regression of zonal wind stress anomalies with respect to the 2008 to 2017 climatology onto the reconstructed NEUC time series for two different wind products (Fig. S6). The regression pattern of both wind products generally agree. Differ-

ences in the wind stress products may arise from the different kind of data that is used. Another source of uncertainty may be different Bulk formulas used for the wind stress calculations, which can result in an uncertainty up to 20% (Large & Yeager, 2004).

In the linear regression patterns, easterly wind stress anomalies between 12°S and 6°N east of about 25°W are leading the NEUC transports by one to two months. Along the equator, these easterly wind stress anomalies may trigger equatorial Kelvin waves. These Kelvin waves may remotely generate Rossby waves traveling as far as 5°N, 23°W by reflecting at the eastern boundary into Rossby waves and coastal trapped waves traveling northward along the coast and generating Rossby waves when the topography is turning north. Rossby waves at 5°N, 23°W may also be generated locally (Burmeister et al., 2016; Foltz et al., 2010). In the ASCAT and JRA-55 data easterly wind stress anomalies above the NEUC region with decreasing magnitude towards the north lead the NEUC transports by two months. The decreasing zonal wind stress indicates changes in the wind stress curl, which may locally generate Rossby waves altering the NEUC flow. Furthermore local zonal wind stress anomalies along the northern coastline of the Gulf of Guinea can trigger westward propagating coastal trapped waves which again generate Rossby waves radiating from the coast when the topography turns north (Chu et al., 2007). In general, the relative low coefficient of correlation ($R<0.45$) suggest that the wind stress field can only explain some part of the NEUC variability and other processes must contribute.

References

Bentamy, A., & Fillon, D. C. (2012). Gridded surface wind fields from Metop/ASCAT measurements. *Int. J. Remote Sens.*, *33*(6), 1729–1754. doi: 10.1080/01431161.2011.600348

Brandt, P., Funk, A., Tantet, A., Johns, W. E., & Fischer, J. (2014). The Equatorial Undercurrent in the central Atlantic and its relation to tropical Atlantic variability. *Clim. Dyn.*, *43*(11), 2985–2997. doi: 10.1007/s00382-014-2061-4

Burmeister, K., Lübbecke, J. F., & Brandt, P. (2016). Revisiting the cause of the eastern equatorial Atlantic cold event in 2009. *J. Geophys. Res. Ocean.*, *7*(121), 4777–4789. doi: 10.1002/2016JC011719

Burmeister, K., Lübbecke, J. F., Brandt, P., & Duteil, O. (2019). Variability of the Atlantic North Equatorial Undercurrent and its impact on oxygen. *J. Geophys. Res. Ocean.*, *in review*(X), X.

Chu, P. C., Ivanov, L. M., Melnichenko, O. V., & Wells, N. C. (2007). On long baroclinic Rossby waves in the tropical North Atlantic observed from profiling floats. *J. Geophys. Res.*, *112*(C5), C05032. doi: 10.1029/2006JC003698

Fischer, J., Brandt, P., Dengler, M., Müller, M., & Symonds, D. (2003). Surveying the upper ocean with the ocean surveyor: A new phased array Doppler current profiler. *J. Atmos. Ocean. Technol.*, *20*(5), 742–751. doi: 10.1175/1520-0426(2003)20⟨742:STUOWT⟩2.0.CO;2

Foltz, G. R., & McPhaden, M. J. (2010). Interaction between the Atlantic meridional and Niño modes. *J. Geophys. Res.*, *37*(18), L18604. doi: 10.1029/2010GL044001

Hahn, J., Brandt, P., Greatbatch, R. J., Krahmann, G., & Körtzinger, A. (2014). Oxygen variance and meridional oxygen supply in the Tropical North East Atlantic oxygen minimum zone. *Clim. Dyn.*, *43*(11), 2999–3024. doi: 10.1007/s00382-014-2065-0

Hahn, J., Brandt, P., Schmidtko, S., & Krahmann, G. (2017). Decadal oxygen change in the eastern tropical North Atlantic. *Ocean Sci.*, *13*(4), 551–576. doi: 10.5194/

193 os-13-551-2017

194 Hsin, Y. C., & Qiu, B. (2012). Seasonal fluctuations of the surface North Equatorial
195 Countercurrent (NECC) across the Pacific basin. *J. Geophys. Res. Ocean.*, *117*(6),
196 1–17. doi: 10.1029/2011JC007794

197 Jochum, M., & Malanotte-Rizzoli, P. (2004). A New Theory for the Generation of the
198 Equatorial Subsurface Countercurrents. *J. Phys. Oceanogr.*, *34*(4), 755–771. doi:
199 10.1175/1520-0485(2004)034⟨0755:ANTFTG⟩2.0.CO;2

200 Kobayashi, S., Ota, Y., Harada, Y., Ebita, A., Ota, Y., Moriya, M., Onoda, H., Onogi,
201 K., Kamahori, H., Kobayashi, C., Endo, H., Miyaoka, K., & Takahashi, K. (2015).
202 The JRA-55 Reanalysis: General Specifications and Basic Characteristics. *J. Met.*
203 *Soc. Jap.*, *93*(1), 5–48. doi: 10.2151/jmsj.2015-001

204 Large, W. G., & Yeager, S. (2004). Diurnal to decadal global forcing for ocean and sea-ice
205 models: The data sets and flux climatologies. *NCAR Technical Note NCAR/TN-*
206 *460+STR*. doi: 10.5065/D6KK98Q6

Table S1. Meridional ship sections taken between 21°W and 26°W from 2002 to 2018. All sections cover at least the upper 350 m from 0°N to 10°N. For all sections ADCP data is available. Sections including oxygen (O_2) and hydrography (CTD) measurements are marked accordingly.

cruise	date	averaged longitude	latitude	O_2/CTD
Meteor 55	Oct-Nov 2002	24°W	0°-10°N	no
Ronald H. Brown A16N	Jun-Aug 2003	26°W	6°S-10°N	no
Ronald H. Brown PNE6	Jun 2006	23°W	5°S-13.5°N	yes
Ronald H. Brown PNE6	Jun-Jul 2006	23°W	5°S-14°N	yes
Meteor 68/2	Jun-Jul 2006	23°W	4°S-14°N	yes
L'Atalante IFM-GEOMAR 4	Feb 2008	23°W	2°S-14°N	yes
L'Atalante IFM-GEOMAR 4	Mar 2008	23°W	2°S-14°N	no
Ronald H. Brown PNE09	Jul-Aug 2009	23°W	0°-14°N	no
Meteor 80/1	Oct-Nov 2009	23°W	6°S-14°N	yes
Meteor 81/1	Feb-Mar 2010	21°W	6°S-13°N	no
Ronald H. Brown PNE10	May 2010	23°W	0°-14°N	yes
Maria S. Merian 18/2	May-Jun 2011	23°W	0°-14°N	no
Ronald H. Brown PNE11	Jul-Aug 2011	23°W	0°-14°N	no
Maria S. Merian 22	Oct-Nov 2012	23°W	6°S-8°N	yes
Maria S. Merian 22	Oct-Nov 2012	23°W	0°-14°N	no
Ronald H. Brown PNE13a	Jan-Feb 2013	23°W	0°-14°N	no
Ronald H. Brown PNE13b	Nov-Dec 2013	23°W	6°S-14°N	yes
Meteor 106	Apr-May 2014	23°W	6°S-14°N	yes
Polarstern PS88.2	Oct-Nov 2014	23°W	2°S-14°N	yes
Endeavor EN-550	Jan 2015	23°W	2°S-14°N	yes
Meteor 119	Sep-Oct 2015	23°W	5.5°S-14°N	yes
Meteor 130	Aug-Oct 2016	23°W	6°S-14°N	yes
Ronald H. Brown PNE17	Feb-Mar 2017	23°W	4°S-14°N	yes
Meteor 145	Feb-Mar 2018	23°W	6°S-14°N	yes

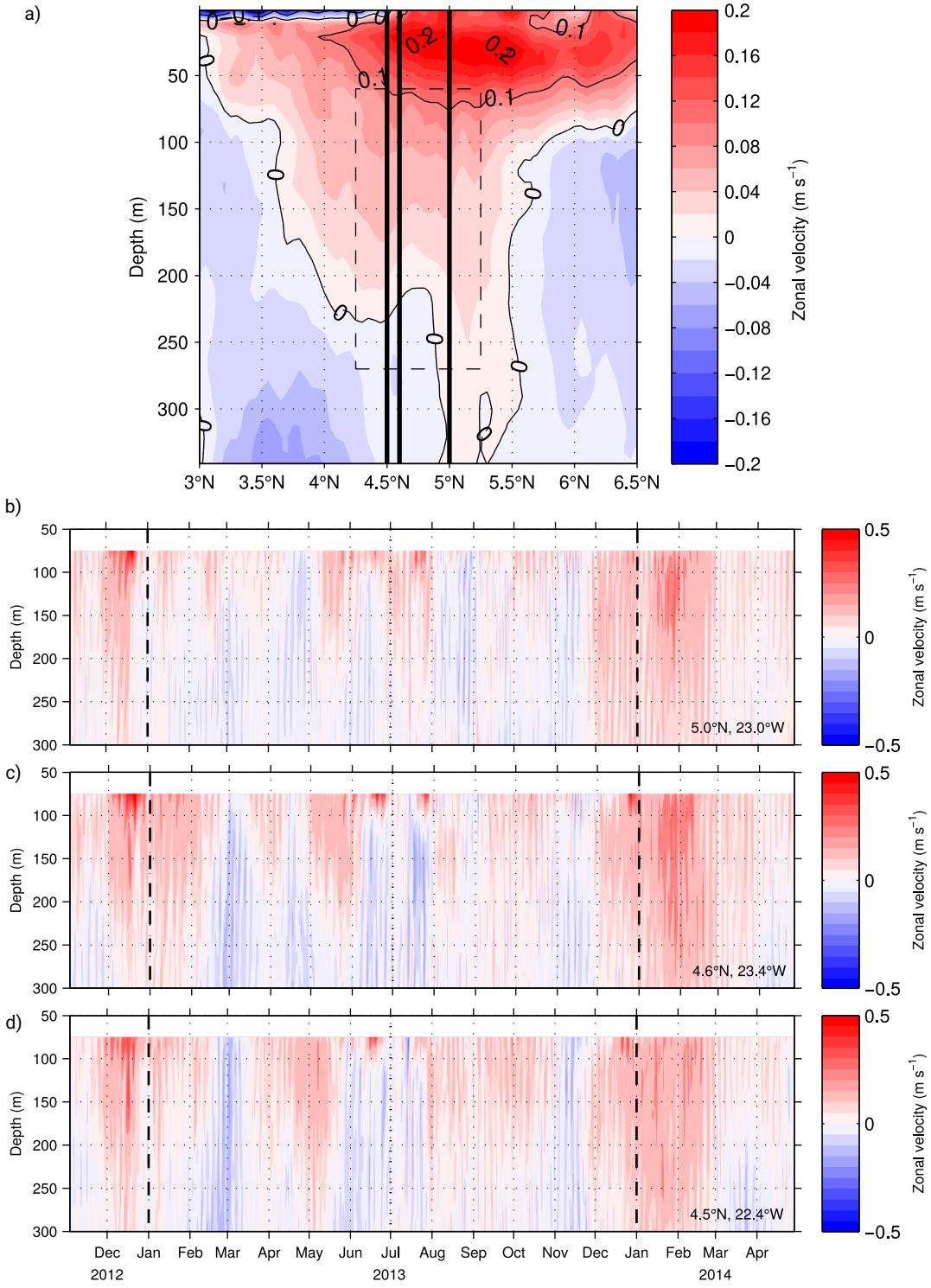

Figure S1. (a) Mean zonal velocity along 23°W estimated on the basis of 24 ship sections taken during 2002 and 2018. Black vertical lines mark the latitudinal position of the three moorings. The black dashed frame marks the box for the transport reconstruction. (b,c,d) Zonal velocity observations at the mooring positions (b) 5.0°N, 23°W, (c) 4.6°N, 23.4°W and (d) 4.5°N, 22.4°W.

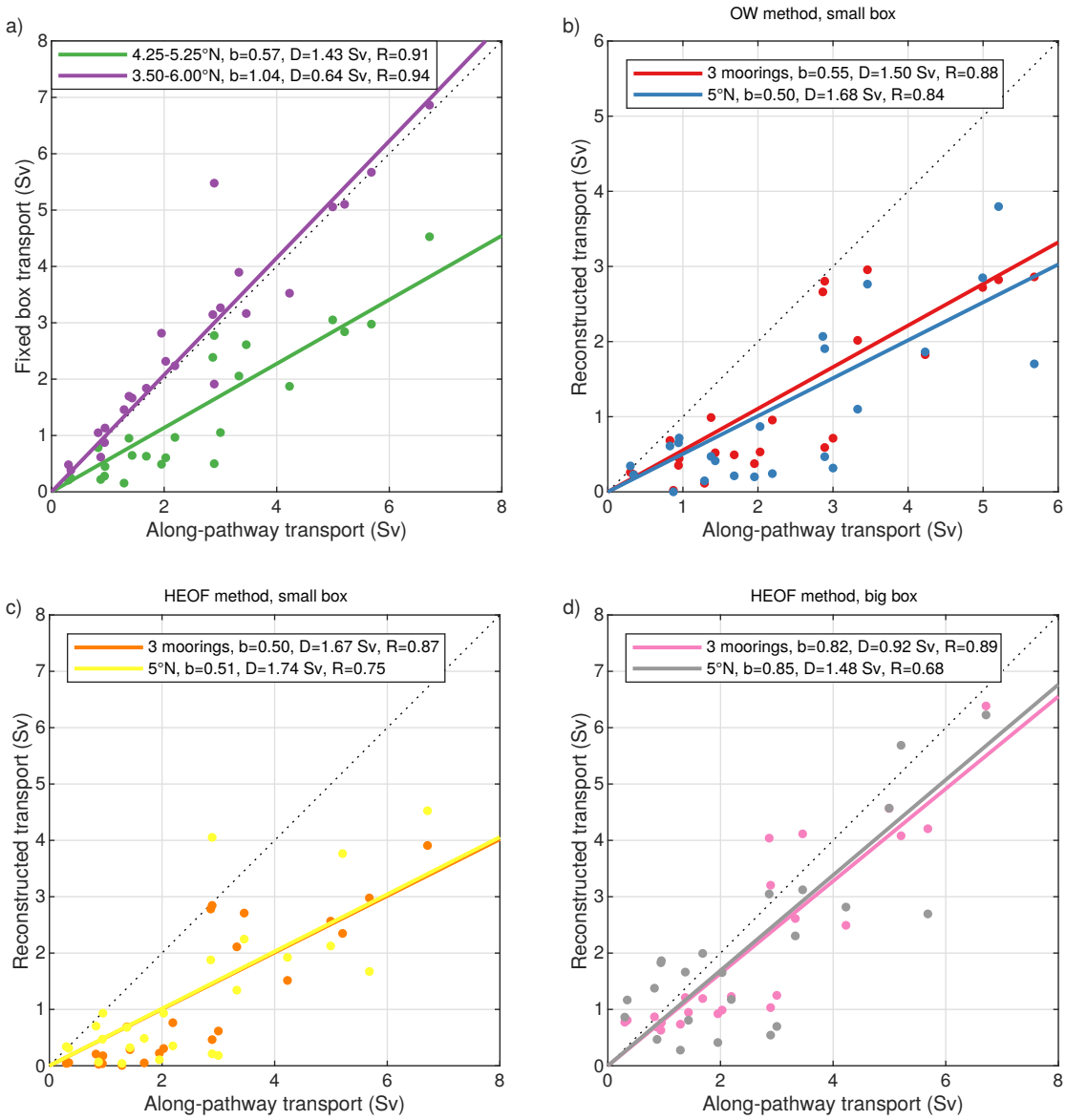

Figure S2. Regression slope b, mean difference D and correlation coefficient R between the reference NEUC transport (along-pathway transport) and the reconstructed transports based on different methods: (a) fixed box integrated transports between 4.25°N and 5.25°N (green) as well as between 3.50°N and 6.00°N (purple), (b) OW method using 3 moorings (red) and only the 5°N mooring, (c) HEOF method using the first HEOF pattern applied to 3 moorings (orange) and only to the 5°N mooring (yellow) for the area between 4.25°N and 5.25°N, (d) HEOF method using the first HEOF pattern applied to 3 moorings (pink) and only to the 5°N mooring (grey) for the area between 3.50°N and 6.00°N.

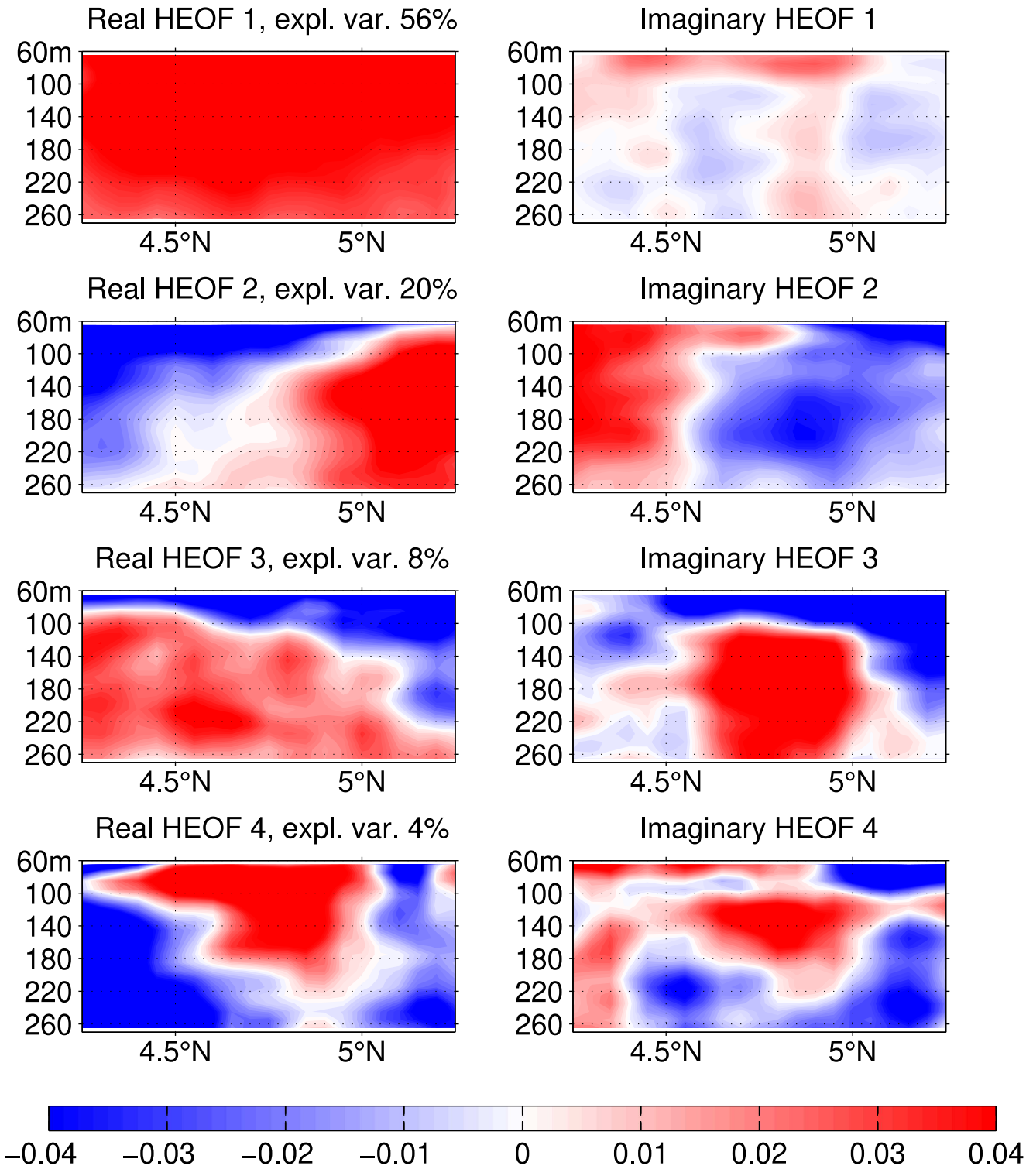

Figure S3. Real (left panels) and imaginary (right panels) dimensionless pattern of the first four Hilbert empirical orthogonal functions calculated from the 24 zonal velocity sections along 23°W between 4.25°N and 5.25°N, 65 m and 270 m depth.

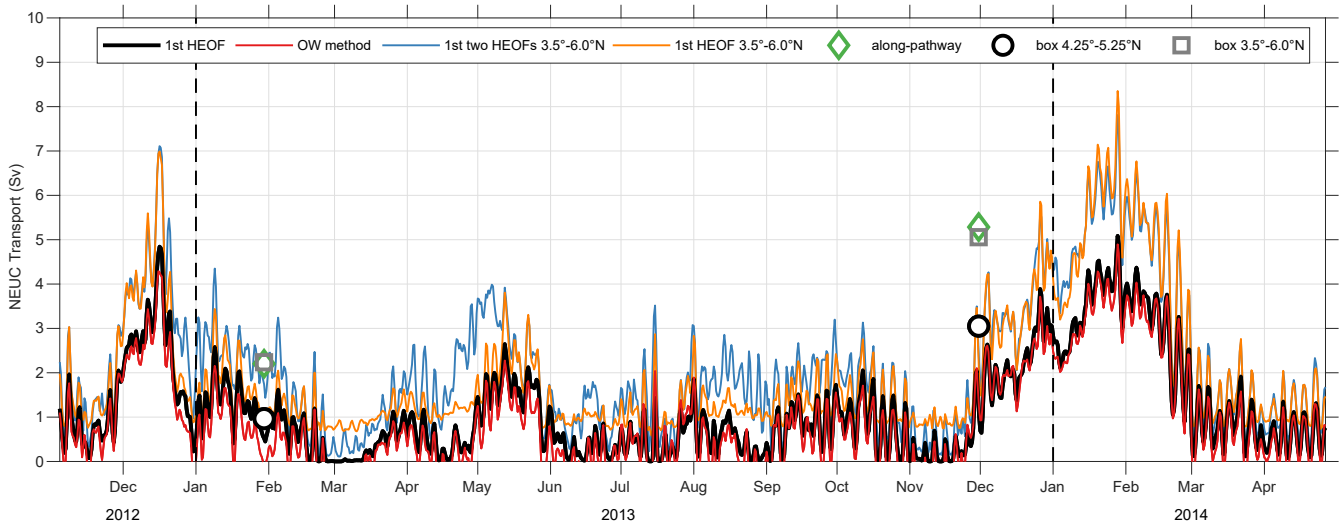

Figure S4. NEUC transport at 23°W calculated by different methods: (i) from ship observations using a path following algorithm (green diamonds); (ii) from ship sections by integrating the eastward velocities in a fixed box between 4.25°N and 5.25°N (black circles) and 3.5°N and 6.0°N (grey squares); (iii) by the HEOF method combining ship sections and moored zonal velocities at three mooring positions using the first HEOF of velocities between 4.25°N and 5.25°N (black line) as well as using the first (orange line) or the first two (blue line) HEOF of velocities between 3.5°N and 6.0°N; (iv) by the OW method combining ship sections between 4.25°N and 5.25°N and moored zonal velocities at three mooring positions (red line).

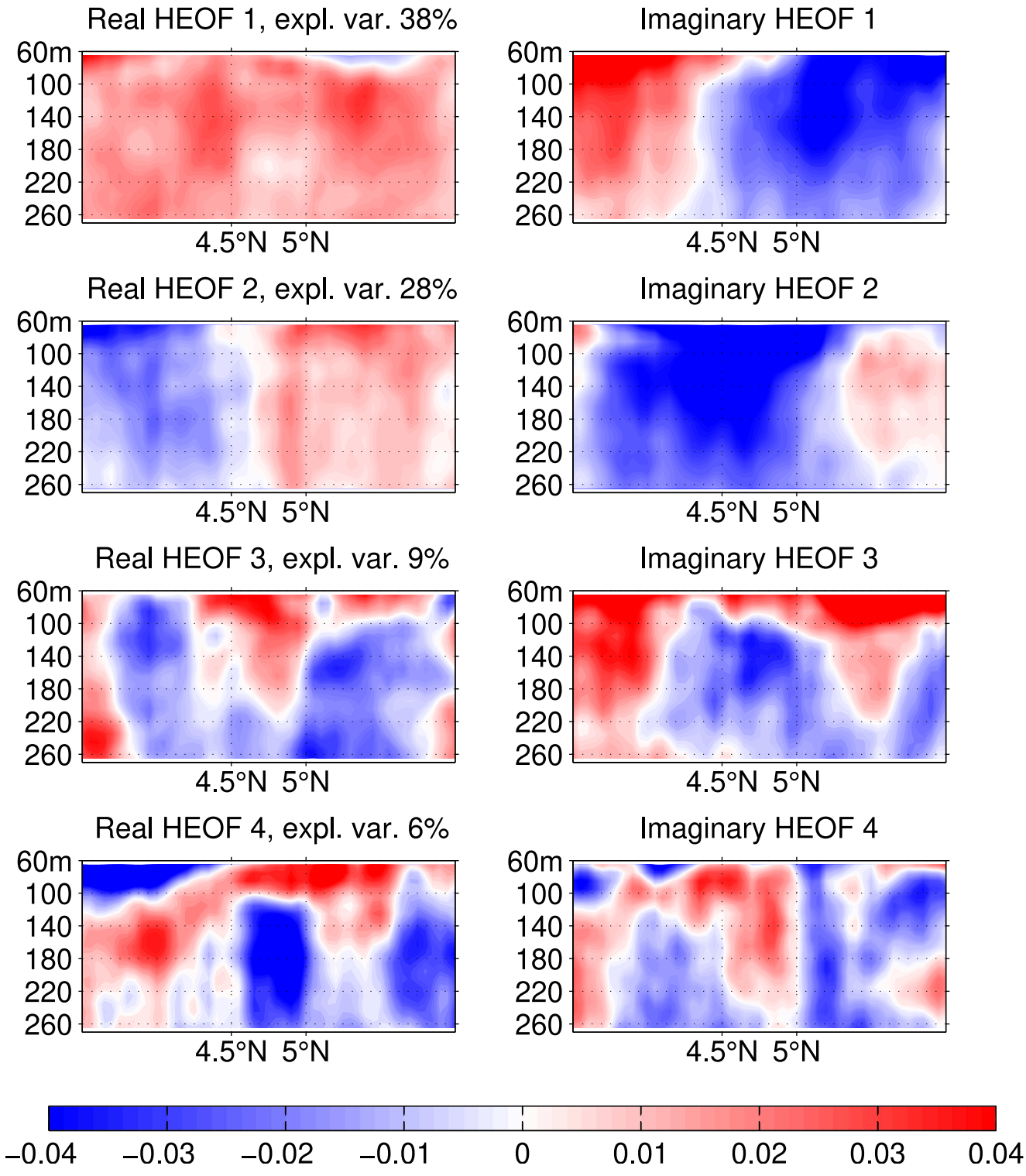

Figure S5. Real (left panels) and imaginary (right panels) dimensionless pattern of the first four Hilbert empirical orthogonal functions calculated from the 24 zonal velocity sections along 23°W between 3.5°N and 6.0°N, 65 m and 270 m depth.

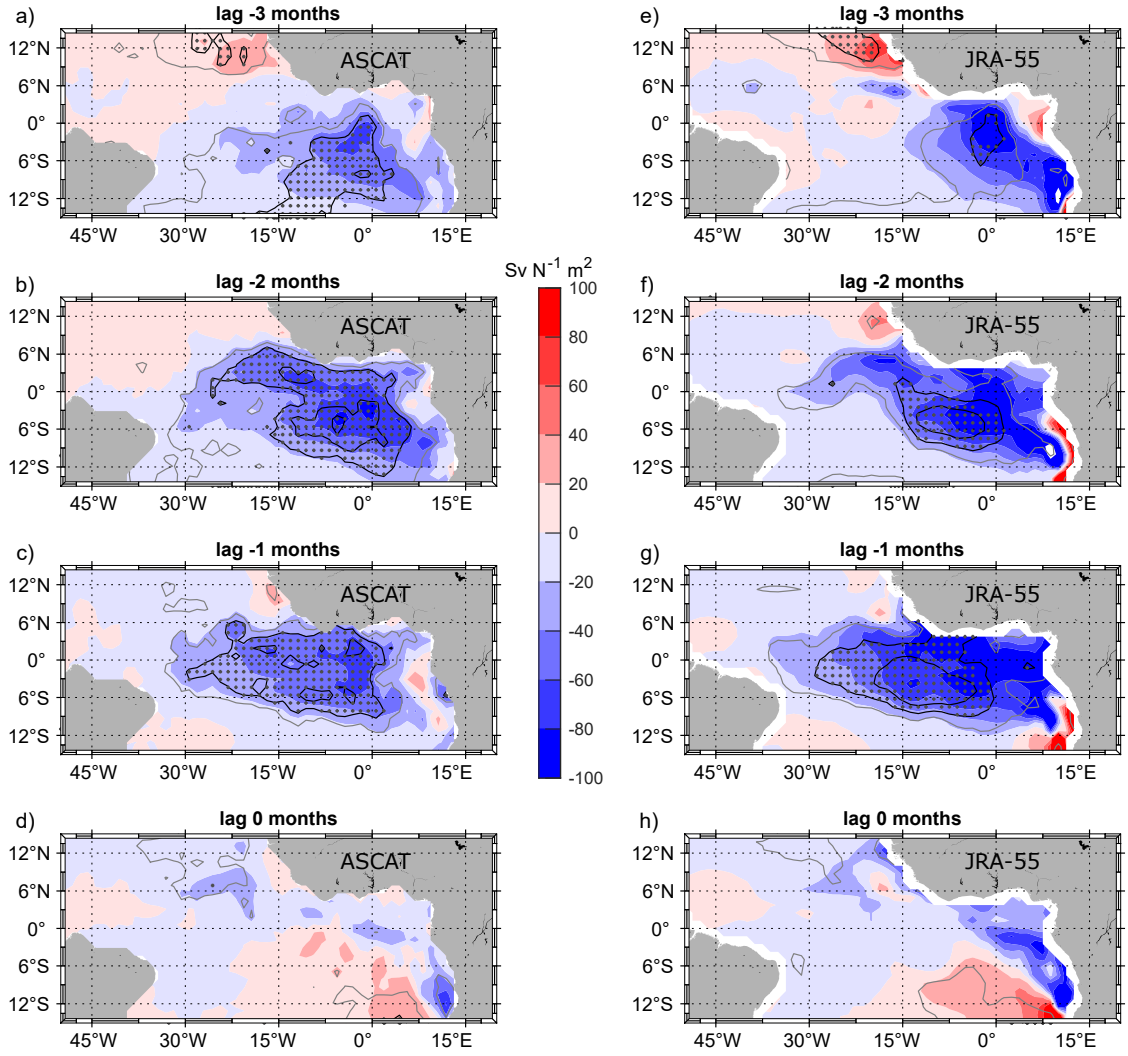

Figure S6. Slope of lead-lag regression of monthly mean zonal wind stress anomalies with respect to the 2008-2017 climatology onto the reconstructed monthly mean NEUC transport time series. Results are shown for ASCAT (a-d) and JRA-55 reanalysis (e-h). Contour lines show the coefficient of correlation (R) with an interval of 0.1, the grey contour marks R=0.1. Grey crosses mark significant values of R.

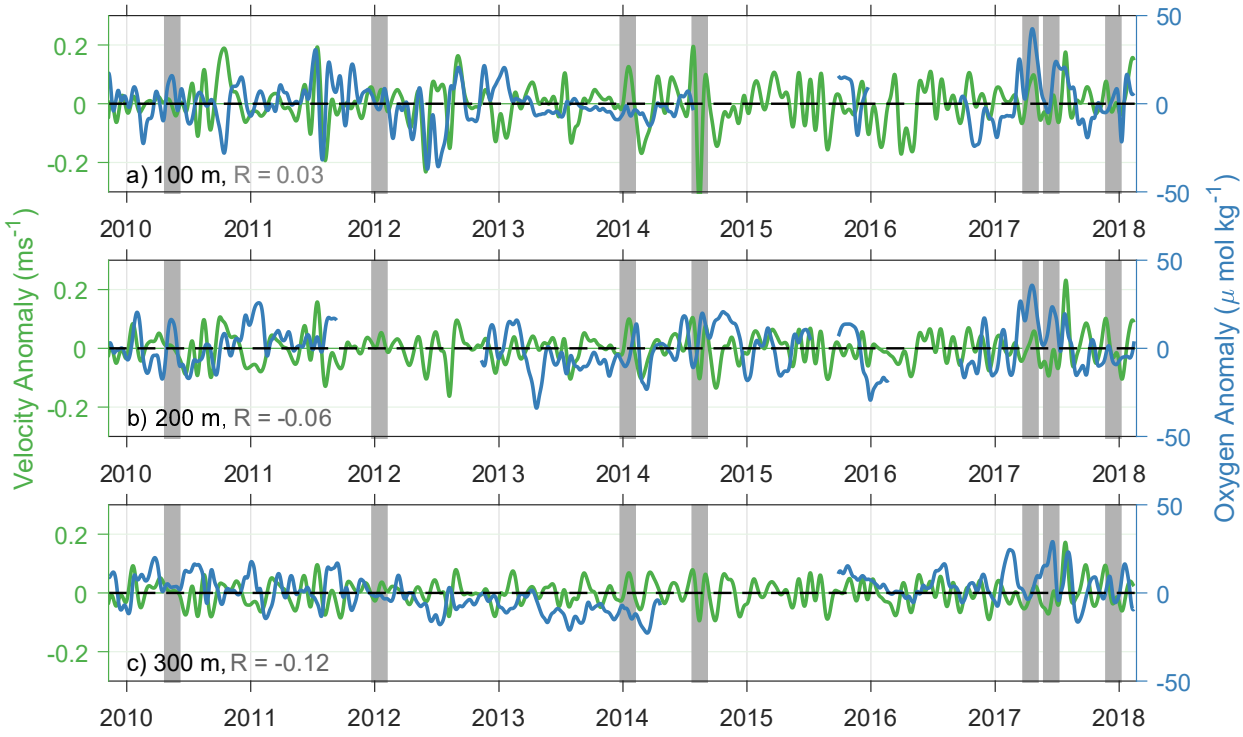

Figure S7. 30-day low-pass filtered (a-c) meridional velocity anomalies (green lines) and oxygen anomalies (blue lines) at 5°N, 23°W at a depth of (a) 100 m, (b) 200 m, and (c) 300 m. Grey bars mark strong NEUC events. The correlation coefficient R at zero lag is not significant on a 95% confident interval.